

## Comparing large-scale 3D Gauss-Newton and BFGS CSEM inversions

Anh Kiet Nguyen, Janniche Iren Nordskog, and Torgeir Wiik\*, Statoil Research Center

Astrid Kornberg Bjørke, Linus Boman, Ole Martin Pedersen, Joseph Ribaud, and Rune Mittet, EMGS

### Summary

Electromagnetic signals are exponentially attenuated in conductive media. Thus, marine controlled-source electromagnetic (CSEM) data where the source and the receivers are located in the water column has exponentially low sensitivity towards the deep stratigraphy, compared to the shallow stratigraphy. In addition, CSEM inversions are also highly non-linear and ill-posed. It is therefore often difficult to achieve good inversion results for the deeper part of the subsurface using gradient based inversion methods.

In this abstract, we describe a large-scale 3-dimensional anisotropic Gauss-Newton (3DGN) CSEM inversion implementation and discuss its advantages over gradient based algorithms. We also show, by synthetic and real data case studies, the large improvements in the 3DGN inversion results compared to those from the Broyden–Fletcher–Goldfarb–Shanno (BFGS) algorithm.

### Introduction

CSEM is a method for remotely measuring the resistivity of the subsurface (Cox, 1980; Chave and Cox, 1982). Its sensitivity towards thin resistive layers has sparked a large interest in the hydrocarbon exploration and exploitation industry (Eidesmo *et al.*, 2002; Ellingsrud *et al.*, 2002; Constable, 2010; Løseth *et al.*, 2015). CSEM data are typically inverted into resistivity models for interpretation and integration with other geophysical data.

Geophysical data inversion problems are typically non-linear and ill-posed (Tarantola, 1987; Zhdanov, 2002). Many distinct different models fit the measured data within the measurement uncertainties. Furthermore, for a vertically propagating plane wave, the electric field amplitude decays as  $|E| \sim |E_0|e^{-z/\delta}$ . Here  $E_0$  is a constant,  $z$  is the depth and the electromagnetic skin depth  $\delta \approx 500\sqrt{\rho/f}$  where  $\rho$  is the formation resistivity and  $f$  is the frequency. The inversion ambiguity together with the exponential sensitivity variations cause large problems for all gradient based inversion algorithms when it comes to CSEM data. High sensitivity leads to large updates close to the sources and receivers, trapping the CSEM inversions into local minima where the responses from deep buried resistive bodies are projected into shallow artificial anomalies.

Sensitivity enhancement methods are typically based on some assumptions, like properties of a background model. However, due to the strong exponential attenuation of the EM signal, a small error in the model used to estimate the sensitivity causes large errors in the sensitivity compensation, leading to poor inversion results. More advanced gradient based methods, like BFGS, where the Hessian is estimated from the gradients of a limited number of previous iterations, may improve the inversion results. However, as we will show below, the Gauss-Newton algorithm provides superior inversion results for CSEM data when compared to the BFGS algorithm.

Many different inversion algorithms have been employed to invert CSEM data. From simple gradient based methods like conjugated gradient (Commer and Newman, 2008; Zhdanov *et al.*, 2014), to the more advanced BFGS (Zach *et al.*, 2008) to the costly Hessian/Gauss-Newton based method (Li *et al.*, 2011; Sasaki, 2013) have been tested on CSEM data. To our knowledge, studies using Hessian/Gauss-Newton tools on full-scale 3D CSEM data sets have not been published. 2.5-dimensional Gauss-Newton inversion implementations have provided very good inversion results when the geology is close to 2-dimensional, examples are Hansen and Mittet (2009); Key (2012); Tseng *et al.* (2015); Wiik *et al.* (2015).

### Theory

We now turn our attention to the theoretical aspects of Gauss-Newton CSEM inversions. We first define a cost function  $\varepsilon(\sigma)$

$$\varepsilon(\sigma) = \varepsilon_d(\sigma) + \lambda \varepsilon_m(\sigma)$$

where  $\sigma$  is the conductivity. The subscripts  $d$  and  $m$  denote data and model, respectively, and  $\lambda$  is a regularization strength parameter. The data misfit is defined as a weighted difference between observed and modelled data

$$\varepsilon_d(\sigma) = |\Delta \mathbf{F}|^2$$

where the complex difference-field vector  $\Delta \mathbf{F} = \mathbf{F}^{synt} - \mathbf{F}^{obs}$ , the super-scripts *synt* and *obs* denote synthetic and observed, respectively. The  $i$ -component of the weighted field  $F_i = E_i/\Delta E_i$  where  $E_i$  is one electromagnetic field data point and  $\Delta E_i$  is the measurement uncertainty and noise associated to that data point (Maaø and Nguyen, 2010; Mittet and Morten, 2012). The regularization term

## Large-scale 3D Gauss-Newton CSEM inversion

$\varepsilon_m(\sigma)$  is used to stabilize the underdetermined inversion problem (Tarantola, 1987; Zhdanov, 2002).

The model update for the data contribution only using the steepest descent method is

$$\Delta\sigma = -\gamma\mathbf{g} = -2\gamma\text{Re}\{\mathbf{J}^\dagger\Delta\mathbf{F}\}$$

where  $\gamma$  is the step length to be determined through a line search along the gradient direction  $\mathbf{g}$ .  $\mathbf{J}$  is the Jacobian and  $\dagger$  is the complex conjugate. Within the first Born approximation, the  $ij$ -element of the Jacobian  $J_{ij} = \frac{dF_i}{d\sigma_j} \sim G(s, \sigma_j)G(\sigma_j, r)$  where  $G(s, \sigma_j)$  is a Green's function from source  $s$  to model element  $\sigma_j$  and  $G(\sigma_j, r)$  a Green's function from  $\sigma_j$  back to the receiver  $r$ . We see already here that the data sensitivity towards a deep buried  $\sigma_j$  is exponentially attenuated on the way down from source to  $\sigma_j$  and then once more on the way back to the receiver. Furthermore, for an order of magnitude estimate of  $\Delta\mathbf{F}$ , let us assume that  $\mathbf{E}^{obs}$  represent data from a background model while  $\mathbf{E}^{synt}$  represent data from the same background model with a small  $d\sigma_j$  perturbation. Then  $E_i^{synt} - E_i^{obs} \sim G(s, \sigma_j)G(\sigma_j, r)$ . Thus, the suggested model update suffers four exponentially damping terms (Green's functions) in the gradient descent method. This leads to a huge sensitivity difference between a shallow buried  $\sigma_j$  from a deep buried  $\sigma_j$ . Given that CSEM inversion is highly non-linear and underdetermined, this sensitivity difference often causes undesirable inversion results using gradient based algorithms.

The model update for the data contribution only using the Gauss-Newton algorithm is

$$\Delta\sigma = -\gamma(2\text{Re}\{\mathbf{J}^\dagger\mathbf{J}\})^{-1}\mathbf{g}$$

Here, we see that the sensitivity problem in the gradient update direction is preconditioned with  $\mathbf{J}^\dagger\mathbf{J}$  which takes into account attenuation and geometrical spreading. Similar arguments have also been put forward in Causse *et al.*, (1999) for seismic full-waveform inversion. The Gauss-Newton algorithm provides, thus, much better sensitivity balancing than gradient-based algorithms for CSEM inversion.

### Method

Setting up and solving the Gauss-Newton equation for a large-scale CSEM dataset and model is a formidable computational task. In order to obtain a computational cost for a Gauss-Newton inversion that is similar to a Quasi-Newton inversion we exploit 1) the sparsity of the Jacobian

and 2) that limited sensitivity allows for a much lower number of inversion parameters than modelling parameters. The decoupling of modelling and inversion parameters is done through a mapping that reduces the number of unknowns with one order of magnitude. The mapping also functions as an implicit regularization.

Even when the sparsity of the Jacobian has been considered, the Jacobian is still too large to fit in memory on typical high performance computer nodes. We therefore use a hybrid MPI/OMP parallel implementation where the Jacobian is distributed on several nodes. In a gradient based method, it is not necessary to do a forward modelling for each source point (Støren *et al.*, 2008), however in order to compute the Jacobian matrix, one forward modelling for each source position is necessary. For maximum efficiency, the distribution of workload on the nodes is done with a graph partitioning scheme using the SCOTCH library (Chevalier and Pellegrini, 2008), which distributes load based on the number of non-zero elements in the Jacobian, and how many Green's function files that must be read on each node. More details of our implementation will be provided in a later publication (L. Boman, personal communication, 2016).

In order to illustrate the improved inversion results obtained with Gauss-Newton, compared with BFGS, we now consider two test cases, one with synthetic data and one with real data. The inversions were full azimuth 3D anisotropic. However, only the vertical resistivity results are presented due to the abstract length limit.

### Synthetic data example

In this section, we show a comparative study between the 3DGN and the BFGS algorithm using a synthetic data set we have called Circus.

The Circus model, shown in Figure 1a and 1b, has two targets: A shallow target about 850 m below the seabed (2400 m below sea level), which is 100 m thick and has a resistivity of 12  $\Omega\text{m}$ , and a deeper target at about 1700 m below the seabed (3300 m below sea level), having a resistivity of 50  $\Omega\text{m}$  and a thickness of 50 m. The deeper target is placed mainly below the shallower target, and this relative position of the targets is chosen since experience show that stacked targets are challenging to image in a BFGS inversion. The water depth varies from 1000 m to 1800 m, and there are several layers of resistivity increasing with depth. Artificial noise was added to the simulated data with a multiplicative noise standard deviation of 0.02, and this noise level was also used in calculating the data weights in the inversion.

## Large-scale 3D Gauss-Newton CSEM inversion

Data from 60 receivers was inverted; see the receiver layout in Figure 1a. Source-receiver offset ranges up to 12 km were included, in total 901 source points along 4 towlines. The horizontal  $E_x$  and  $E_y$  electric fields were inverted for 4 frequencies between 0.1 and 1.0 Hz, giving a total of 142000 data points in the inversion. The start model used in the inversion tests is shown in Figure 1c. It has a simple resistivity profile increasing with depth, but contains no structural information.

The BFGS inversion images one anomaly at a depth approximately 3000 m below sea level, see Figure 1. The result shown was obtained in 77 iterations (including line searches) and has an RMS misfit of 0.92. The Gauss-Newton inversion images the two targets, one at 2400m depth (below sea level), and one at 3200 m depth. The result shown was obtained in 12 Gauss-Newton iterations, and has an RMS misfit for the data of 0.92.

Figure 1 clearly shows the improvement in the inversion results from the Gauss-Newton algorithm compared to the BFGS algorithm. Due to the large sensitivity difference, the BFGS algorithm has fitted the data by updating the very shallow sections right below the receivers, taking the inversion path from the initial model into a less favorable local minimum where the important anomalies are not imaged properly. The 3DGN algorithm on the other hand leads the inversion into a better local minimum where the updates are more balanced and thereby correctly split the two anomalies and places them at the correct location.

### Real data example

In this section, we show 3DGN and BFGS inversion results for the 3D Snøhvit CSEM dataset acquired in 2010 through the EDDA consortium. Snøhvit is a gas/condensate field located in the central part of the Hammerfest Basin in the Barents Sea. The water depth is around 300 m. The depth of the reservoirs varies between 2000-2500 m. We use the horizontal electric fields  $E_x$  and  $E_y$  with the frequencies 0.5, 1.0 and 2.0 Hz with 11000, 9000 and 8000 m maximum source-receiver offset, respectively. The number of inversion parameters is 563000, the number of data points amount to 160000.

The initial model is created by a simple three-layer model; water, upper formation and lower formation separated by the seabed and the Base Cretaceous Unconformity (BCU). We populate the upper and lower formations with vertical resistivity of 6 and 20  $\Omega\text{m}$ , and horizontal resistivity of 3 and 5  $\Omega\text{m}$ , respectively. The models are then smoothed before used in the inversion. The BFGS inversion used 100 iterations, including line search, to reach a RMS data misfit of 0.92. The 3DGN inversion used 5 Gauss-Newton

iterations to reach a data misfit of 1.2. The multiplicative data uncertainty (Maaø and Nguyen, 2010) is set to 5%. The additive noise is estimated based on statistical stacking variances of short FFT windows as part of the data pre-processing.

Figure 2 shows the initial, BFGS and 3DGN inverted vertical resistivity models. To reduce the dominance of the resistive anomalies with peaks above 300  $\Omega\text{m}$ , we show the models in logarithmic scale. We see that the BFGS result contains many resistive anomalies right below the receivers. We believe that is due to the sensitivity problem discussed in the theory section. Consequently, the resistivity anomaly that should have been at the Snøhvit reservoir is reduced in strength. In the Albatross case, it is not reconstructed at all. On the other hand, we see that 3DGN has reconstructed the southern Albatross anomaly. Furthermore, 3DGN has much stronger update of the Snøhvit anomaly compared to BFGS, 300 versus 100  $\Omega\text{m}$ , respectively. The difference is clearly visible even in a logarithmic color scale. The resistivity value for the Snøhvit anomaly is also much more consistent with resistivity logs for the 3DGN case. The origin of the resistivity anomaly in the area between Albatross and Snøhvit is at present still unknown.

### Conclusions

We have described a large-scale 3D anisotropic Gauss-Newton CSEM inversion implementation and discussed its advantages compared to gradient based implementations. The case studies on synthetic and real data show a large improvement in the results when compared to results from the gradient based BFGS algorithm when everything else is equal. 3DGN inversion was able to construct the resistive anomalies at the correct depths with much more accurate resistivity values.

The synthetic Circus case shows that while the BFGS inversion is not able to separate the two stacked targets the 3DGN inversion correctly images the two targets at correct depths. In addition, BFGS also creates an erroneous low resistivity layer right under the receivers.

The Snøhvit real data case shows that 3DGN reconstruct the smaller Albatross anomaly while BFGS does not, for the given initial model. Furthermore, the Snøhvit anomaly mapped by 3DGN is much stronger and more consistent to resistivity logs, compared to the resistivity anomaly from the BFGS inversion. In addition, BFGS creates many artificial resistive anomalies right beneath the receivers.

# Large-scale 3D Gauss-Newton CSEM inversion

## Acknowledgments

We thank the Research Council of Norway for supporting this work through PETROMAKS program. We thank Statoil and EMGS for the permissions to publish the results, and Statoil for the seismic data used in the study. We also thank Emmanuel Causse, Jan-Petter Morten and Kristian Rymann Hansen for stimulating discussions.

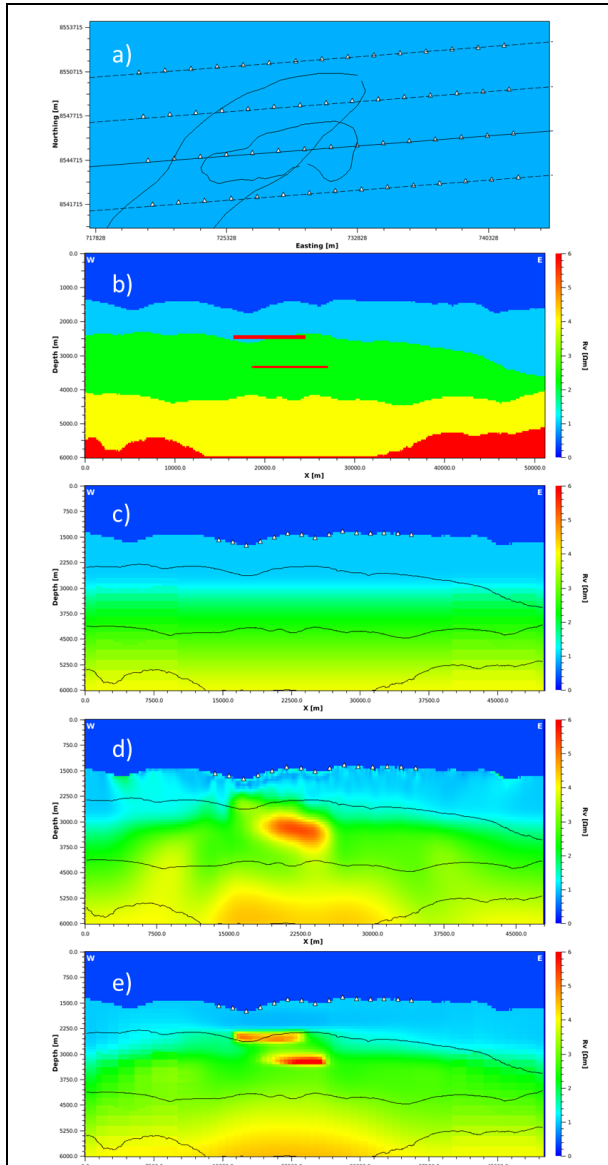


Figure 1: Synthetic data example a) Survey layout and target outlines. The lines show the towlines, the solid line the line shown in the figures b-e. b) The true model used to generate the Circus data set. c) Initial model used in the inversions. d) BFGS inversion result e) 3DGN inversion result. Notice that both inversions were run anisotropic, but only the vertical resistivity models are shown.

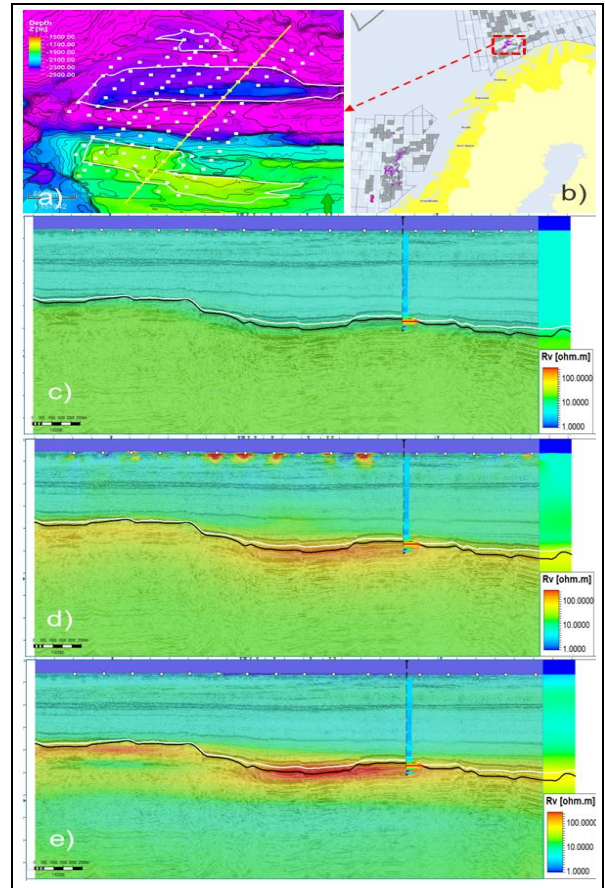


Figure 2: a) Receiver and discovery outlines, from bottom to top: Albatross, Snøhvit and Snøhvit north. Color indicates depth of BCU which coincide with top reservoir. Yellow line shows the position of the sections in c,d and e. b) geographic location of the Snøhvit field. c), d) and e) initial, BFGS inverted and 3DGN inverted vertical resistivity models in log scale, overlaid the seismic section. Well log of the horizontal resistivity is also shown in c, d and e.

## EDITED REFERENCES

Note: This reference list is a copyedited version of the reference list submitted by the author. Reference lists for the 2016 SEG Technical Program Expanded Abstracts have been copyedited so that references provided with the online metadata for each paper will achieve a high degree of linking to cited sources that appear on the Web.

## REFERENCES

- Causse, E., R. Mittet, and B. Ursin, 1999, Preconditioning of full-waveform inversion in viscoacoustic media: *Geophysics*, **64**, no. 1, 130–145. <http://dx.doi.org/10.1190/1.1444510>.
- Chave, A. D., and C. S. Cox, 1982, Controlled electromagnetic sources for measuring electrical conductivity beneath the oceans: Part 1 — Forward problem and model study: *Journal of Geophysical Research*, **87**, B7, 5327–5338. <http://dx.doi.org/10.1029/JB087iB07p05327>.
- Chevalier, C., and F. Pellegrini, 2008, PT-SCOTCH: a tool for efficient parallel graph ordering: *Parallel Computing*, **34**, no. 6-8, 318–331. <http://dx.doi.org/10.1016/j.parco.2007.12.001>.
- Commer, M., and G. A. Newman, 2008, New advances in three-dimensional controlled-source electromagnetic inversion: *Geophysical Journal International*, **172**, no. 2, 513–535. <http://dx.doi.org/10.1111/j.1365-246X.2007.03663.x>.
- Constable, S., 2010, Ten years of marine CSEM for hydrocarbon exploration: *Geophysics*, **75**, no. 5, A67–A81. <http://dx.doi.org/10.1190/1.3483451>.
- Cox, C., 1980, Electromagnetic induction in the oceans and inferences on the constitution of the earth: *Geophysical Surveys*, **4**, no. 1-2, 137–156. <http://dx.doi.org/10.1007/BF01452963>.
- Eidesmo, T., S. Ellingsrud, L. M. MacGregor, S. Constable, M. C. Sinha, S. Johansen, F. N. Kong, and H. Westerdahl, 2002, Seabed Logging (SBL), a new method for remote and direct identification of hydrocarbon filled layers in deepwater areas using controlled source electromagnetic sounding: *First Break*, **20**, 144–152.
- Ellingsrud, S., T. Eidesmo, S. Johansen, M. C. Sinha, L. M. MacGregor, and S. Constable, 2002, Remote sensing of hydrocarbon layers by seabed logging SBL: Results from a cruise offshore Angola: *The Leading Edge*, **21**, no. 10, 972–982. <http://dx.doi.org/10.1190/1.1518433>.
- Hansen, K. R., and R. Mittet, 2009, Incorporating seismic horizons in inversion of CSEM data, 79<sup>th</sup> Annual International Meeting, SEG, Expanded Abstracts, 694–698, <http://dx.doi.org/10.1190/1.3255849>.
- Key, K., 2012, Marine EM inversion using unstructured grids: A 2D parallel adaptive finite element algorithm: 82<sup>nd</sup> Annual International Meeting, SEG, Expanded Abstracts, <http://dx.doi.org/10.1190/segam2012-1294.1>.
- Li, M., A. Abubakar, J. Liu, G. Pan, and T. M. Habashy, 2011, A compressed implicit Jacobian scheme for three-dimensional electromagnetic data inversion: *Geophysics*, **76**, no. 3, F173–F183. <http://dx.doi.org/10.1190/1.3569482>.
- Løseth, L. O., J. O. Hansen, T. Wiik, M. Roudot, B. Dubois, A. K. Nguyen, and L. B. Henriksen, 2015, CSEM pre-well predictions in the Johan Castberg Area, Barents Sea: 77<sup>th</sup> Conference and Exhibition, EAGE, Extended Abstracts, <http://dx.doi.org/10.3997/2214-4609.201413218>.
- Maaø, F. A., and A. K. Nguyen, 2010, Enhanced subsurface response for marine CSEM surveying: *Geophysics*, **75**, no. 3, 7–10. <http://dx.doi.org/10.1190/1.3377054>.
- Mittet, R., and J. P. Morten, 2012, Detection and imaging sensitivity of the marine CSEM method: *Geophysics*, **77**, no. 6, E411–E425. <http://dx.doi.org/10.1190/geo2012-0016.1>.
- Sasaki, Y., 2013, 3D inversion of marine CSEM and MT data: an approach to shallow-water problem: *Geophysics*, **78**, no. 1, E59–E65. <http://dx.doi.org/10.1190/geo2012-0094.1>.
- Støren, T., J. J. Zach, and F. A. Maaø, 2008, Gradient calculations for 3D inversion of CSEM data using a fast finite-difference time-domain modelling code: 70<sup>th</sup> Conference and Exhibition, EAGE, Extended Abstracts, P 194.

- Tarantola, A., 1987, *Inverse Problem Theory*: Elsevier.
- Tseng, H.-W., J. Stalnaker, L. M. MacGregor, and R. V. Ackerman, 2015, Multi-dimensional analyses of the SEAM controlled source electromagnetic data—the story of a blind test of interpretation workflows: *Geophysical Prospecting*, **63**, no. 6, 1383–1402. <http://dx.doi.org/10.1111/1365-2478.12327>.
- Wiik, T., J. I. Nordskag, E. Ø. Dischler, and A. K. Nguyen, 2015, Inversion of inline and broadside marine controlled-source electromagnetic data with constraints derived from seismic data: *Geophysical Prospecting*, **63**, no. 6, 1371–1382. <http://dx.doi.org/10.1111/1365-2478.12294>.
- Zach, J. J., A. K. Bjørke, T. Støren, and F. Maaø, 2008, 3D inversion of marine CSEM data using a fast finite-difference time-domain forward code and approximate hessian-based optimization: 78<sup>th</sup> Annual International Meeting, SEG, Expanded Abstracts, 614–618, <http://dx.doi.org/10.1190/1.3063726>.
- Zhdanov, M. S., 2002, *Geophysical Inverse Theory and Regularization Problems*: Elsevier.
- Zhdanov, M. S., M. Endo, D. Yoon, M. Cuma, J. Mattsson, and J. Midgley, 2014, Anisotropic 3D inversion of towed-streamer electromagnetic data: Case study from the Troll West oil province: *Interpretation (Tulsa)*, **2**, no. 3, SH97–SH113. <http://dx.doi.org/10.1190/INT-2013-0156.1>.